Mechanics of Advanced Composite Structures

Journal homepage: https://macs.semnan.ac.ir/

Semnan University

ISSN: 2423-7043

Research Article

Experimental Evaluation of the Effect of Combining a Two-Phase Nano-Composite Containing AL_2O_3 and NbC in a Surface-Coated Resin Matrix: a Study Based on Dielectric Losses and Radar Reflectance

Mohammad Khakbaz[a], Mehrdad Motavasselolhagh[b], Masoud Javadi[c*], Reza Sarkhosh[d]

[a] *Department of Aerospace Engineering, Faculty of Graduate education, Shahid Sattari University of Aeronautical Sciences and Technology, Tehran, Iran*

[b] *School of Mechanical Engineering, Iran University of Science and Technology, Tehran, Iran*

[c*] *Assistant Professor, Department of aerospace engineering, shahid sattari University of Aeronautical sciences and technology, Tehran, Iran*

[d] *Assistant Professor, Department of aerospace engineering, shahid sattari University of Aeronautical sciences and technology, Tehran, Iran*

ARTICLE INFO

Article history:

Received:

Revised:

Accepted:

Keywords:

Electromagnetic wave;
Absorption;

Dielectric loss;

Polymer nano-composites;
Al_2O_3/NbC biphasic system.

ABSTRACT

Electromagnetic wave-absorbing polymer nano-coatings are recognized as important for advanced electromagnetic shielding and wave management applications. In this study, a novel two-phase Al_2O_3/NbC polymer nano-composite within an epoxy resin matrix is introduced, incorporating dual silane surface treatments (APTMS and GPTMS) to enhance interfacial bonding and ensure uniform dispersion of the reinforcing materials. A designed experimental (DOE) plan was implemented before the fabrication process to determine the optimal weight fractions of aluminum oxide (Al_2O_3) and niobium carbide (NbC). Subsequently, chemical bonding, particle surface modification, and matrix homogenization were performed, and the samples were prepared in rectangular molds suitable for electromagnetic rectangular wave guide measurements in the 8.2–12.5 GHz range. The structural and chemical characteristics were analyzed using X-ray diffraction (XRD), Fourier-transform infrared spectroscopy (FTIR), and scanning electron microscopy (SEM). The results obtained from electromagnetic absorption and reflection measurements within the 8.2–12.5 GHz frequency range show that sample No.1, with a higher NbC content, demonstrates stronger absorption near 9.5 GHz but reduced performance at higher frequencies. Sample No.2, containing a balanced ratio of Al_2O_3 and NbC, exhibits a more uniform response across the frequency range, while sample No.3, with a higher Al_2O_3 fraction, presents improved impedance matching, enhanced dielectric loss, and absorption exceeding 80% throughout 8.2–12.5 GHz, accompanied by a reflection reduction of approximately 6%. These results indicate that tuning the weight fraction of the two phases allows optimization of broadband absorption performance. Overall, the dual-phase Al_2O_3/NbC system with surface-modified particles can achieve efficient, broadband electromagnetic absorption, offering potential for advanced shielding and wave control applications for aerospace industries.

1. Introduction

With the rapid growth of electrical and electronic devices, the development of materials capable of absorbing electromagnetic waves has

*** Corresponding author.**
E-mail address: mohammadi@gmail.com

Cite this article as:

become a major focus of commercial and military research. Materials that can absorb a portion of the electromagnetic wave incident on a surface and convert it into wasted thermal energy [1]. Radar cloaking is an advanced technology in this field that reduces the probability of detection by enemy radar by minimizing the radar cross-section (RCS). Currently, two main approaches are used to achieve this goal: first, modifying the object's geometry to reduce reflection at specific angles, and second, utilizing radar-absorbing materials (RAM) to absorb electromagnetic energy. On the other hand, in advanced systems such as fighter jets, supersonic aircraft, and missiles, the temperature of some components during operation may reach 700 °C or higher. Therefore, the design and fabrication of stable RAMs at high temperatures has become an unavoidable necessity [2-4]. Metal-ceramic composite coatings are attractive options for this purpose due to their properties, such as abrasion resistance, specific conductivity, thermal shock resistance, and mechanical stability at high temperatures. These coatings can be produced by methods such as co-deposition, sol-gel, hot pressing, and thermal spraying [3-6]. Among various materials, niobium carbide has gained a special place due to its high melting point, good strength, chemical stability, and desirable wear resistance. However, the production of NbC coatings using plasma spraying technology is accompanied by challenges such as low deposition efficiency, incomplete melting of powders, high porosity, and the occurrence of microstructural defects. To overcome these limitations, the use of NbC-Al_2O_3-SiC composite powders and the plasma spraying method can lead to significant improvement of microstructure and an increase in mechanical properties[7]. Also, NbB_2-NbC-Al_2O_3 coatings have been reported to have high microhardness, suitable toughness, and desirable abrasion resistance, the main reason for which is the better melting of the powder in the presence of Al_2O_3 nanoparticles[8]. Meanwhile, the coatings obtained from in-situ reaction by the plasma spraying method also form a dense structure with the presence of coaxial NbB_2 nanocrystals, spherical NbC particles, and α-Al_2O_3 phase. This phase heterogeneity creates distinct boundaries and even transitional phases due to the diffusion of elements, which overall improves the toughness[9]. Studies have shown that Al_2O_3 as a dielectric phase in ceramics[10], or in combination with manganese ore powder[11], and also with polymers such as polypyrrole[12], has a high ability to absorb electromagnetic waves. On the other hand, NbC, as a magnetic phase, when combined with carbon sources such as bamboo powder in the carbothermal reduction process[13] or with phases such as SnC[14], can provide high electrical conductivity, which helps to increase the efficiency of wave absorption. In addition, NbC as a ceramic reinforcement in W-NbC composites increases toughness and ultimate strength[15]. Niobium carbide has also become one of the most important high-temperature amplifiers due to its special properties, such as a very high melting point (3600 °C), a density of 7.79 g/cm3 (less than 19.25 for tantalum), a Vickers hardness of 19.6 GPa, and a Young's modulus in the range of 338 to 580 GPa[16]. NbC serves as an excellent high-temperature reinforcement. To cover the absorption mechanism more comprehensively, recent studies demonstrate the importance of both dielectric and magnetic loss pathways as well as structural design (e.g., $Ti_3C_2T_x$/Fe_3O_4/UV resin honeycomb architectures) in achieving bandwidth tuning and enhanced absorption efficiency [17], while others highlight how impedance matching and attenuation constant optimization govern performance in advanced absorbers [18]. In this regard, other reputable research, such as [19-21] have investigated the mechanism of absorption of electromagnetic waves.

In recent years, electromagnetic wave-absorbing polymer coatings with single-phase or multi-phase fillers have been introduced. However, in many studies, precise surface control to create a stable bond between the ceramic phases and the polymer matrix has been less considered, which leads to non-uniform dispersion and reduced adsorption efficiency. Also, numerous studies have been conducted on the absorption and reflection of high-frequency waves, considering composite compounds with Al_2O_3 [22-28].

In the present study, the two-phase combination of NbC and Al_2O_3 was chosen due to its complementary properties. NbC, with its magnetic nature, high conductivity, and large dielectric constant, is the main factor in increasing the conduction loss and enhancing the absorption in the resonance regions; while Al_2O_3, as a dielectric phase, improves the impedance matching and broadens the absorption bandwidth by creating multiple scattering paths. By using controlled silane surface treatment, a stable chemical bond has been established between the particles and the epoxy matrix, enabling uniform dispersion and preventing particle aggregation. This approach not only allows the intensity and location of the absorption peaks to be tuned by changing the NbC/Al_2O_3 ratio, but also enables the achievement of broadband and stable absorption in the X-band. In addition, the design of such coatings can pave the way for the development of

a new generation of lightweight, high-temperature-resistant, and multipurpose absorbent materials. Next, in the second section, the governing relations for extracting the electromagnetic response and dielectric properties, as well as modeling the effective environment method and investigating the effects of chemical alignment, are stated. In the third section, the experimental design method is stated. The description of the experimental tests is presented in the fourth section. In the fifth section, the experimental test results are presented. In the last section, the achievements of this research are presented. These achievements open up new prospects for applications beyond radar stealth, such as space structures and electromagnetic shielding in advanced industries.

2. Mathematical Modeling

The electromagnetic properties of NbC/Al_2O_3 composites in epoxy resin depend on multiphase complexities, surface interactions, and frequency dispersion phenomena. In these systems, conductive NbC and dielectric Al_2O_3 phases are distributed throughout the polymer matrix, often as dispersed particles or continuous networks. Mathematical analysis requires consideration of this distribution, the chemical leveling effects, and the electromagnetic response resulting from the composite structure.

2.1. Electromagnetic Response and Dielectric Properties

The electromagnetic behavior of multiphase composites is defined by considering the complex dielectric response in Eq.1. The complex dielectric constant, as a fundamental parameter, includes a real part related to energy storage and an imaginary part representing energy dissipation:

$$\varepsilon(\omega) = \varepsilon'(\omega) - j\varepsilon''(\omega) \quad (1)$$

where ε'(ω) represents the electrical energy storage capacity and ε″(ω) represents the energy dissipation at angular frequency ω. The imaginary unit j specifies the phase difference between the electric field and the electric displacement. Similarly, the magnetic response of the composite, especially in the presence of NbC particles with weak ferromagnetic properties, is described by the complex magnetic permeability in Eq.2 [29]:

$$\mu(\omega) = \mu'(\omega) - j\mu''(\omega) \quad (2)$$

Energy loss in the composite is quantified through the dielectric loss factor in Equation 3, which represents the ratio of dissipated energy to stored energy.

$$\tan\delta_e(\omega) = \varepsilon''(\omega) / \varepsilon'(\omega) \quad (3)$$

This parameter is directly related to the efficiency of absorbing electromagnetic waves and converting them into heat. In general, the effective conductivity of the composite is related to the imaginary part of the dielectric constant through Eq.4. This parameter relates to the efficiency with which electromagnetic waves are absorbed and converted into heat. Generally, the effective conductivity of the composite can be linked to the imaginary part of the dielectric constant via Eq.4:

$$\sigma^*(\omega) = \omega\,\varepsilon_0\,\varepsilon''(\omega) \quad (4)$$

where ε_0 is the dielectric constant of vacuum (8.854×10^{-12} F/m) and σ* is the effective conductivity in S/m. The electromagnetic shielding performance of composites is determined based on the interaction of incident waves with the multilayer structure. The characteristic impedance of free space is derived from Eq.5 as a basic reference.

$$Z_0 = \sqrt{(\mu_0/\varepsilon_0)} = 377\ \Omega \quad (5)$$

For a single-layer composite coating with thickness d, the input impedance is a function of the electromagnetic properties of the material and the geometry of the system. For a single-layer composite coating with thickness d, the input impedance depends on the electromagnetic properties of the material and the system's geometry.

$$Z_{in} = Z_0\sqrt{(\mu_r/\varepsilon_r)}\coth(\gamma d) \quad (6)$$

where $\mu_r=\mu/\mu_0$ and $\varepsilon_r=\varepsilon/\varepsilon_0$ are the relative permeability and relative dielectric constant, respectively. γ is the propagation constant, and $k=\omega/c$ is the wavenumber in vacuum. The impedance mismatch between free space and the composite leads to a reflection of a portion of the incident waves, which is described by the reflection coefficient in equation 7:

$$\Gamma = (Z_{in} - Z_0)/(Z_{in} + Z_0) \quad (7)$$

The total electromagnetic attenuation (SE), which is the basic measure of protection performance, is calculated through the logarithmic ratio of incident to transmitted field strength in Eq.8 [30-32]:

$$SE = 20\log_{10}(E_i/E_t) \quad (8)$$

2.2. Effective Environment Theory Modeling

The spatial arrangement of NbC and Al_2O_3 phases within the resin matrix influences the composite's effective electromagnetic properties. In systems with randomly distributed spherical particles, the Maxwell-Garnett model defines the relationship between the properties of the individual components and the effective properties of the composite, as expressed in the following Eq.9 [33]:

$$\varepsilon_{eff} = \varepsilon_m[(\varepsilon_i + 2\varepsilon_m + 2f(\varepsilon_i - \varepsilon_m))/(\varepsilon_i \quad (9)$$

$$+2\varepsilon_m - f(\varepsilon_i - \varepsilon_m))]$$

In this context, ε_m represents the dielectric constant of the resin matrix, ε_i is the dielectric constant of the filler particles, and f denotes the volume fraction of these particles. This model is generally accurate for low to moderate concentrations of particles. However, for multiphase systems, such as NbC/Al_2O_3 composites, the Bruggeman model provides improved accuracy by accounting for the interactions between different phases.

$$\begin{aligned} &f_{NbC}(\varepsilon_{NbC} - \varepsilon_{eff})/(\varepsilon_{NbC} + 2\varepsilon_{eff}) \\ &+f_{Al_2O_3}(\varepsilon_{Al_2O_3} - \varepsilon_{eff})/(\varepsilon_{Al_2O_3} + 2\varepsilon_{eff}) \\ &+ f_{resin}(\varepsilon_{resin} - \varepsilon_{eff})/(\varepsilon_{resin} + 2\varepsilon_{eff}) \\ &= 0 \end{aligned} \quad (10)$$

where f_{NbC}, $f_{Al_2O_3}$, and f_{resin} are the volume fractions of NbC, Al_2O_3, and resin, respectively, with the constraint $f_{NbC} + f_{Al_2O_3} + f_{resin} = 1$.

2.3. Effects of Chemical Leveling

The surface treatment of NbC and Al_2O_3 particles with silane agents affects the electromagnetic properties of the composite through changes in interphase interactions. The siloxane (Si-O-Si) bonds and Si-O-Nb/Al surface bonds formed during the surface treatment process reduce the interphase resistance and facilitate charge transfer, which is the reference equation for multiphase surface treatment as described in Eq.11:

$$\begin{aligned} \varepsilon_{mo} d_i f_{ie} d &= \varepsilon_{untreate} d \\ &+ \Delta\varepsilon(\Gamma_{silane}, SSA) \end{aligned} \quad (11)$$

where the variable Γ_{silane} represents the surface concentration of silane, measured in mol/m², while SSA refers to the specific surface area of the particles, expressed in m²/g. The changes resulting from surface treatment, denoted as Δε, depend on both the extent of surface coverage and the strength of the bonds formed. The chemical equilibrium governing surface bond formation is influenced by the temperature-dependent equilibrium constant, as outlined in Eq.12:

$$K_{Bond} = K_0 \exp(-E_a/RT) \quad (12)$$

where K_0 is the projection constant, E_a is the bond activation energy in kJ/mol, R is the universal gas constant, and T is the temperature in Kelvin.

3. Design of Experiment (DoE)

The purpose of this experimental design was to optimize the composition and determine the average values suitable for preparing NbC/Al_2O_3/epoxy samples with different weight ratios. The composite data from the experimental design include three targeted NbC/Al_2O_3/epoxy compositions, each replicated three times. Statistical analysis shows that the average values of each component fully match the designed values, and the standard deviation is less than 0.5%, confirming the stability of the mixing process and the uniformity of the composition. The histograms in Fig. 1, showing the normal distribution of the data, display a symmetrical distribution without outliers, indicating the accuracy of nanoparticle weighing and mixing. The regular bell-shaped peaks for Al_2O_3 and NbC s high repeatability of the mass percentage in different samples, while the resin, with negligible dispersion, demonstrates phase stability in the polymer matrix. This statistical behavior confirms that the experimental design was correctly implemented, considering weight constraints and electromagnetic responses, and that the obtained data are statistically valid. Table 1 presents the proposed DOE values as the mass percentage ratios of the materials in three different composite samples, in which the balance between magnetic and dielectric components is maintained to determine the dominant effects on absorption and loss across different material phases at high and low frequencies. Overall, the results demonstrate that the controlled mixing and weighing method successfully reproduced the designed compounds with high accuracy, providing a suitable basis for analyzing EMI properties.

4. Experimental Method

The objective of this laboratory method is to thoroughly describe and implement the production and selection process for silane-coated NbC/Al_2O_3 materials designed for electromagnetic interference (EMI) shielding applications. This involves detailing the entire production process from start to finish, including phase composition, coating, mixing, molding, curing, and performance evaluation. Additionally, it will cover the associated physical mechanisms and chemical reactions involved in these processes.

4.1. Surface Treatment to Construction

In the field of electromagnetic shielding, nano-composites containing NbC and Al_2O_3 are recognized as key options for EMI shielding due to the special combination of electronic properties of NbC, which has a relatively high conductivity, and insulating/mechanical properties and surface stability of Al_2O_3. NbC, with its significant electrical conductivity in the range of 2 to 7,000,000 S/m and high melting temperature, along with its suitable density and ability to be combined with polymer resins, helps to create conductive networks and absorb waves

in different frequency ranges. In contrast, Al_2O_3, with its α-Al_2O_3 crystal structure and high electrical resistivity (>10^{14}Ω·cm), high Young's modulus, and lower density than NbC, acts as an

Table1. Suggested values for experimental design considering three different samples

sample	Component	Ave (wt%)	Std.Dev	Median (wt%)
	Al_2O_3	15.12	0.37	15.12
1	NbC	20.09	0.45	20.30
	Epoxy	64.79	0.27	64.95
	Al_2O_3	20.00	0.35	19.89
2	NbC	14.96	0.27	14.95
	Epoxy	65.04	0.10	65.05
	Al_2O_3	17.50	0.41	17.66
3	NbC	17.45	0.44	17.44
	Epoxy	65.05	0.13	65.09

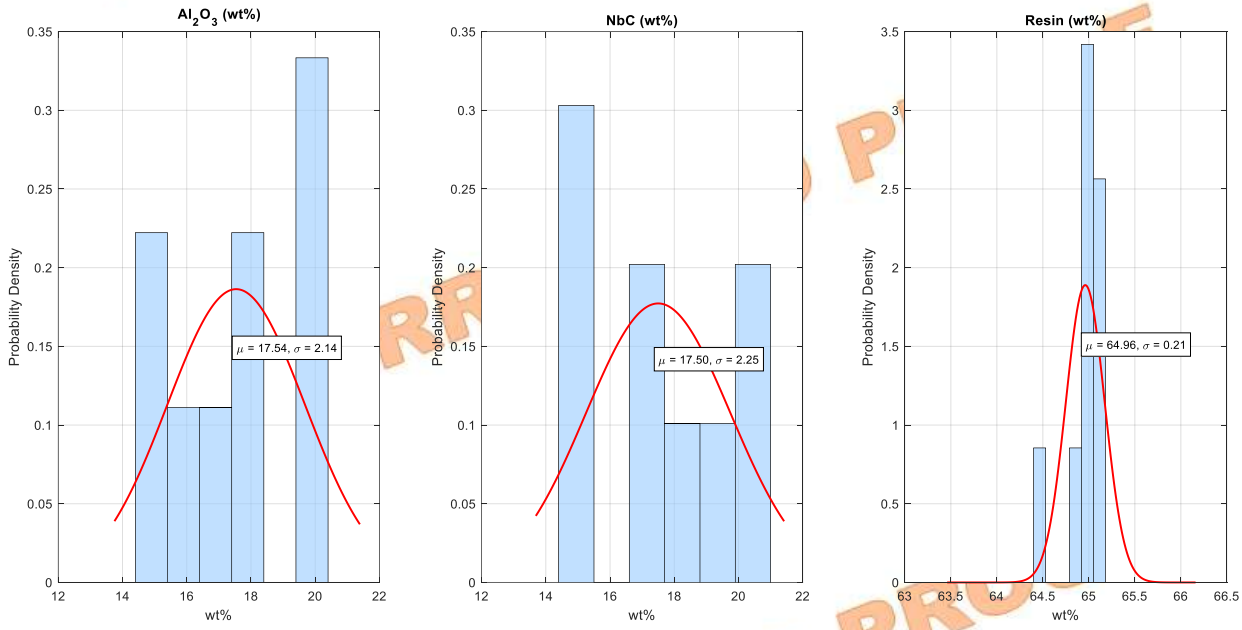

Fig. 1. Normal distribution of experimental data

insulating phase and a catalyst of microstructures that contribute to proper dispersion and mechanical stability. The combination of these two phases in NbC/Al_2O_3 two-phase systems in epoxy resins allows for optimization of the EMI process and maintaining phase stability against radar scattering to achieve desirable properties in terms of EMI absorption, emission, and reflection. Figure 2 provides a summary of the chemical surface treatment process. To achieve this goal, the production process consists of three main parts: (1) preparation and surface treatment of NbC and Al_2O_3 particles, (2) mixing and homogenizing the surface-treated nanoparticles with epoxy resin, and (3) molding and curing process with precise temperature and time control to improve surface bonding, homogeneity in particle distribution, and phase stability. In the first step, surface treatment of NbC is performed with one of the organic silanes such as APTMS (3-aminobutyltrimethoxysilane) to create acceptable Si–O–Nb bonds on the NbC surface. This surface bonding improves the bonding of the NbC phase with the resin, resulting in improved dispersion and electrical contact within the composite. In order to increase surface compatibility and ultimately improve EMI characteristics, surfaced NbC is introduced together with surfaced Al_2O_3 in the epoxy resin compounding process. Surfaced Al_2O_3 with

GPTMS (3-glycidoxypropyltrimethoxysilane) to create a Si–O–Si network and silicate bonds with the resin, increasing phase compatibility and reducing negative interactions between heterogeneous phases. In the following, it is proposed to employ strategies to control the morphology and particle size of surfaced NbC and Al_2O_3 to achieve a more homogeneous distribution in the epoxy resin, reduce radar scattering effects, improve surface bonding, and increase phase stability against curing temperature and humidity. Also, the use of a combination of NbC layered with Al_2O_3 layered is recommended to create conductive networks with the ability to maintain thermal and mechanical stability in the appropriate and more stable EMI frequency spectrum. Semiconductor-electrical studies on the NbC/APTES-GPTMS surface and field investigation of the electrical contacts between NbC and Al_2O_3 layered through methods such as EIS (electrointensity), XPS, and TEM can help to more accurately improve the phase relationship and EMI efficiency. These approaches, while maintaining the process routine, lead to improved EMI absorption, emission, and reflection in the target frequency ranges.

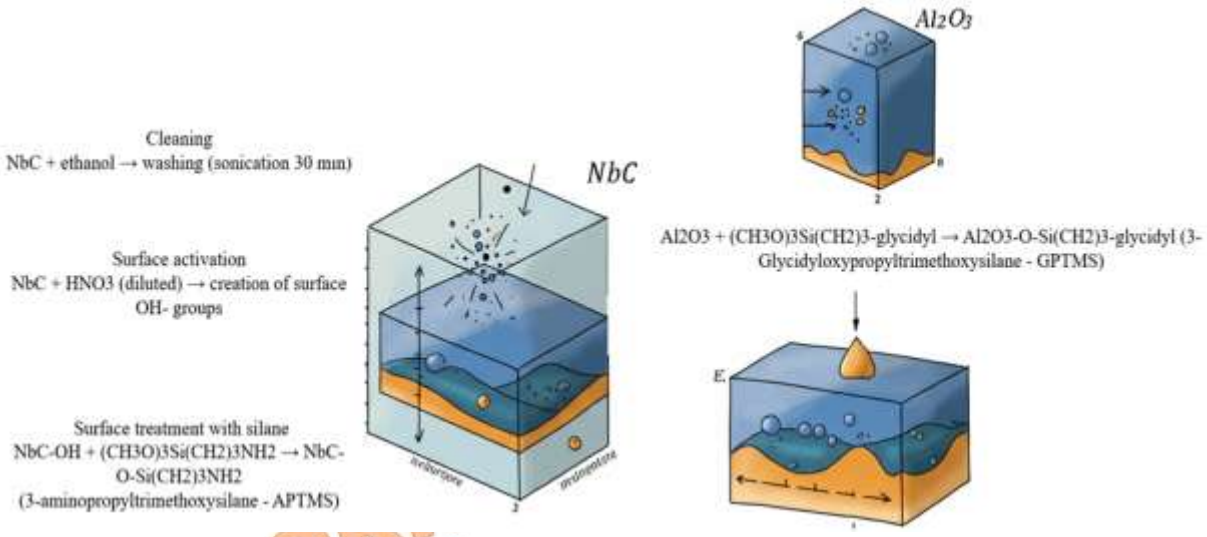

Fig. 2. Chemical surface treatment and surface treatment process of Al_2O_3/NbC nano-composite

In the process of compounding and preparing the base resin, a two-component epoxy resin with a resin-to-hardener ratio of 2:1 by weight is utilized to create a stable polymer compound with desirable mechanical properties. Initially, surface-coated materials are mixed with acetone solvent at a specific mass percentage and then homogenized in an ultrasonic bath. After this, the resin is heated to 120°C and added to the materials, followed by another round of sonication. Subsequently, gentle stirring is performed, and any air is removed under vacuum. The hardener is then added, and the mixture is poured into silicone molds for sample preparation. Figure 3 illustrates the entire process from preparation to the final composite samples.

4.2. Network Analyzer Test

The dielectric constant test is performed to determine the electrical and electromagnetic properties of the composite produced inside the X-band waveguide device[34]. The samples were placed in a VNA device with dimensions of 22.86 × 10.16 equipped with two ports. with a WR-90 interface, and the experiments were performed in the X-band frequency range, which includes the range of 8.2 to 12.5 GHz. After calibrating the system with reference standards, the scattering parameters of each sample were measured to determine their precise electromagnetic reflection and absorption characteristics. To ensure the measurement accuracy, which was targeted at ±0.1 dB, the input power level was carefully controlled to prevent nonlinear effects and signal saturation. The system's time stability and repeatability of the results were investigated, and possible errors related to connections or unwanted reflections were identified and managed. Each sample was tested at different power levels and over the entire frequency range to monitor sensitivity changes and possible nonlinear effects. The data obtained were used for a detailed analysis of the material properties, along with phase and delay studies, and loss and reflection parameters to determine the optimal operating ranges of the system. The measurement configuration was set up so that the second port was considered closed to extract only the effects of absorption and

reflection and to assume zero transmission coefficients.

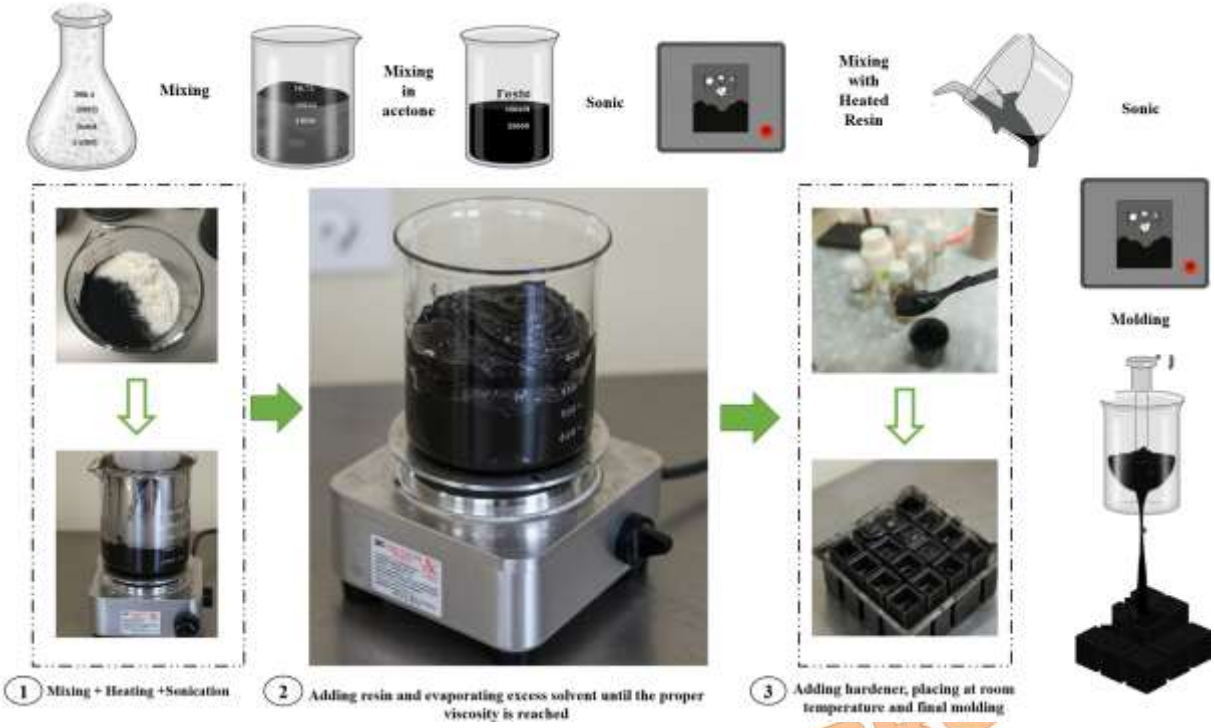

Fig. 3. Process of preparing and Mixing Nanomaterials

This arrangement allowed for a precise separation of the reflection and absorption modes to improve the ability to detect small changes in the dispersion parameters of the nano-composites containing Al_2O_3 and NbC. The accuracy of the wave propagation path and noise reduction at each frequency was graphically examined by S-parameter plots to identify error thresholds by linear and nonlinear analysis of the data set and to investigate the possibility of channel or cable failure before specialized analyses. Figure 4 shows the general schematic of the VNA setup for nano-composite samples.

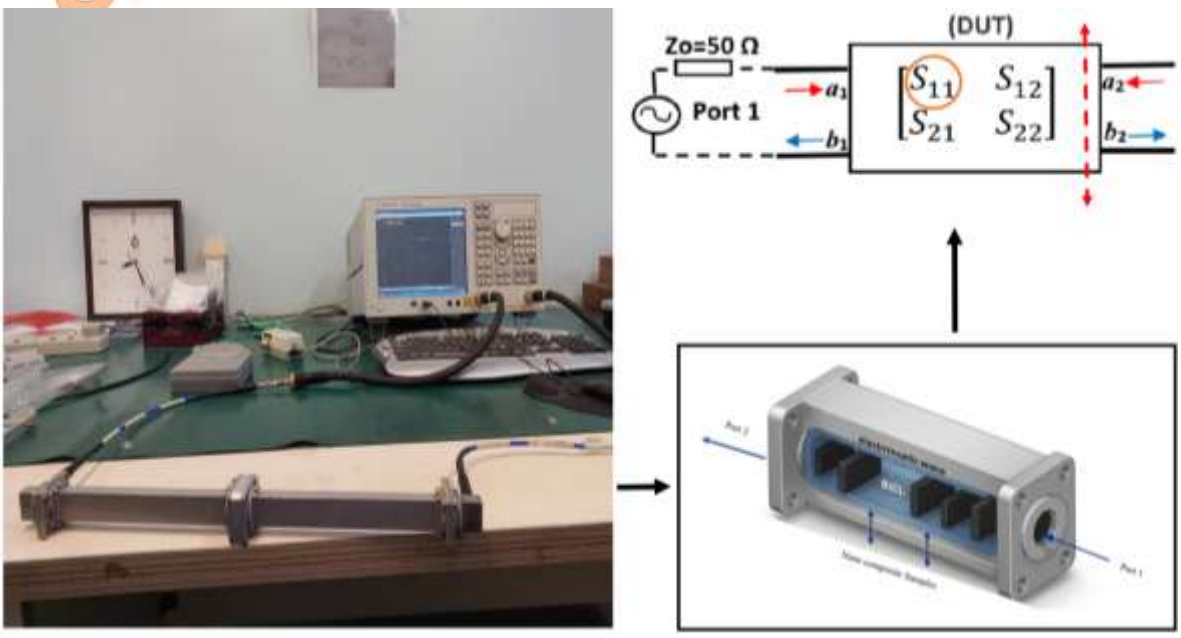

Fig. 4. Experimental setup for X-band electromagnetic measurements using a rectangular waveguide, with sample dimensions of 22.86 × 10.16 mm^2

5. Results

5.1. Electromagnetic Reflection Loss (RL)

The results of the waveguide test in the X-band frequency range are shown in Table 2 and Fig. 5. In the frequency range of 8.2 to 12.4 GHz, sample No.1 with a NbC: Al_2O_3 ratio of 4:3 performs better at lower frequencies, starting at 8.2 GHz with an *RL* of about -8.2 dB and gradually increasing absorption, reaching a minimum of -12 dB at 9.5 GHz. This behavior is due to the simultaneous dielectric resonance caused by NbC particles with surface and multipath scattering of Al_2O_3, and creating an impedance match close to the ideal state of $\mu/\varepsilon \approx 1$. After this point and passing 10 GHz, due to the change in the phase ratio of ε and μ and the departure from the matching condition, a sharp drop in absorption occurs, and the *RL* value increases to -2.8 dB at 11.5 GHz (higher reflection). This indicates that the electromagnetic energy dissipation paths in this sample are mainly active around the mid-frequency range and will be more suitable for applications focused on the 10–9 GHz band. In contrast, the sample No.2 with a 3:4 ratio has a weaker absorption efficiency at low frequencies (starting at -3.4 dB at 8.2 GHz), but with increasing frequency, the effects of interfacial polarization and scattering losses in the composite structure are enhanced, and the upward trend in absorption begins at about 10 GHz. This sample reaches a minimum of -12 dB in the range of 11–11.5 GHz, which is due to the gradual improvement of the impedance matching and the simultaneous resonance of the electric and magnetic components, and remains in an efficient state up to 12 GHz. Such behavior makes sample No.2 an ideal choice for absorption in higher bands and covering the 11–12 GHz spectrum. Sample No.3 with an equal ratio of NbC and Al_2O_3 has a more uniform behavior and remains between -12 dB and -5 dB over most of the frequency range. This relative stability is due to the balance between the dielectric loss of Al_2O_3 and the moderate conductivity of NbC, which prevents the formation of deep absorption peaks. However, around 12.4 GHz, the effects of boundary-capacitance resonance and activation of NbC conduction paths in the Al_2O_3 insulating matrix give rise to a minimum of -10.8 dB, which, although having a very limited bandwidth, can be useful for applications requiring absorption at the upper edge of the band. Overall, the results show that changing the NbC to Al_2O_3 ratio shifts the absorption band and changes the effective bandwidth. Increasing the NbC contribution in the first sample results in a strong absorption peak in the midband but a decrease in performance at high frequencies; decreasing the NbC in the third sample shifts the absorption to a higher band and provides a suitable bandwidth in the 11–12 GHz range; and the equal ratio in the third sample provides a flat response with a late peak that can be converted to a broader absorption by changing the thickness or adjusting the composition.

Table 2. Electromagnetic *RL* in the X-band

Frequency. (GHz)	sample No.1 (*RL*: dB)	sample No.2 (*RL*: dB)	sample No.3 (*RL*: dB)
8.2	-8.2	-3.4	-4.8
8.5	-10.5	-2.1	-6.2
9	-11.8	-6.1	-8.8
9.5	-12	-4.7	-7.5
10	-10.9	-7.8	-9.4
10.5	-6.3	-9.6	-9.1
11	-8.7	-11.2	-8.3
11.5	-2.8	-12	-7
12	-4.1	-11.5	-0.4
12.4	-1.5	-8.8	-10.8

*** Corresponding author.**
E-mail address: mohammadi@gmail.com

Cite this article as:

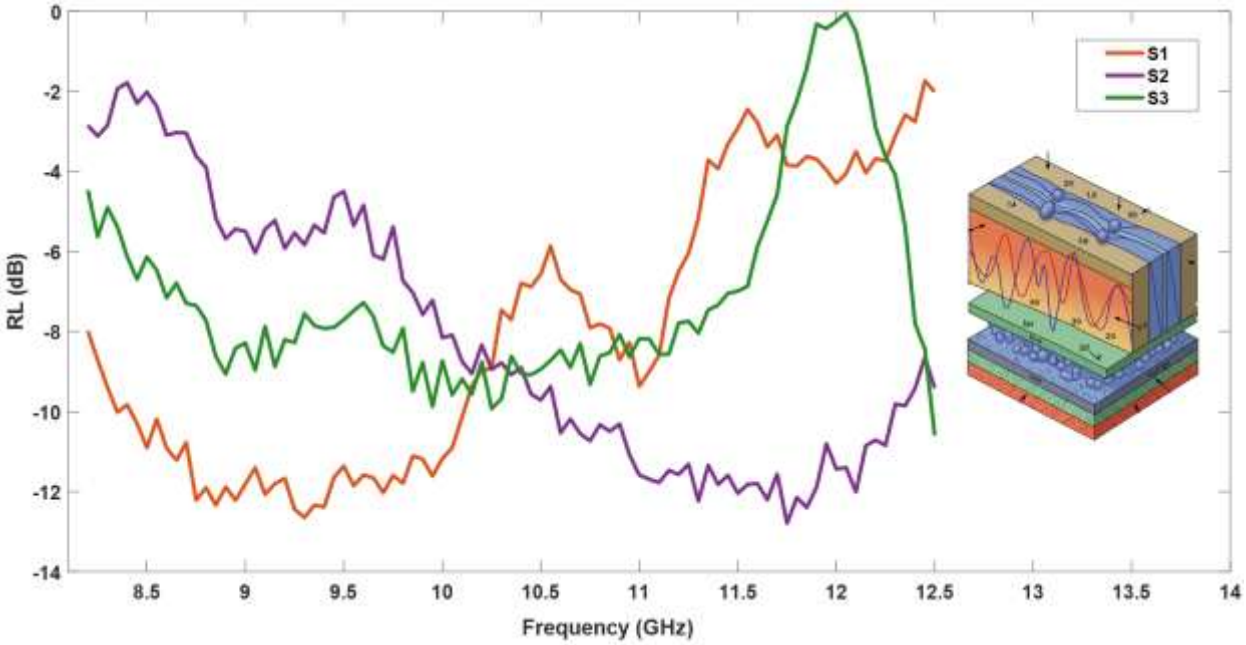

Fig. 5. Reflection loss (*RL*, dB) of the three samples as a function of frequency (GHz)

5.2. Electromagnetic Absorption

As shown in Fig. 6, the absorption value in the X-band range depends strongly on the ratio of the material's constituent components.

Sample No.1, which contains the NbC conductive phase, increases its absorption from 85.5% at 8.2 GHz to a maximum of 93.5% at 9.5 GHz, corresponding to the optimal impedance-matching region. At this frequency, the absorption range varies from a minimum of 66% to a maximum of 100%. This range decreases almost linearly up to 11 GHz, where the absorption varies between 49% and 85%. Beyond this point, the absorption range continues to decrease with increasing frequency, reaching a minimum of 30% at 12.4 GHz.

Sample No.2 shows a reverse trend due to its dominant dielectric behavior. Its absorption begins at 56% at 8.2 GHz and rises steadily to 86% at 12.4 GHz. The absorption variation follows a similar pattern from 8.5 to 12.4 GHz, with the greatest change occurring at 9 GHz (30%). Across the X-band, the lowest and highest absorption values occur at 8.4 and 11.66 GHz, respectively, 39% and 93.5%. These results suggest that polarization losses, rather than conduction or magnetic losses, dominate the attenuation mechanism in this sample. The presence of Al_2O_3 enhances energy dissipation through dipolar relaxation, which becomes most effective in the 10–12 GHz range. This behavior shows that the dielectric matrix suppresses eddy current losses while maintaining moderate impedance balance, making this sample suitable for absorber configurations requiring stable, frequency-selective performance.

In sample No.3, the absorption variation across the X-band is larger than in the previous two samples. It begins with an absorption of 68% at around 8.2 GHz and reaches its maximum variation at 12 GHz, with a change of approximately 80%. The highest absorption is observed at 12.4 GHz (about 91.5%), while the lowest occurs at 12 GHz (about 10%). These results show that absorption control in this model offers greater flexibility. This suggests that microstructural uniformity and percolation pathways play key roles in achieving consistent absorption performance. It also indicates that the interplay between conduction and dielectric losses is frequency-dependent, which can be exploited in designing hybrid absorbers with tailored band gaps. Furthermore, this highlights the importance of precise compositional control and the need to account for nonlinear behavior in absorber design. Finally, calculating the average reflection over the entire frequency range indicates that fine-tuning the NbC-to-Al_2O_3 ratio can optimize both bandwidth and absorption strength for specific frequency windows. Overall, the results show that the electromagnetic behavior of NbC–Al_2O_3 composites is highly tunable and governed by a balance of conduction, polarization, and interfacial effects, making these materials strong candidates for next-generation radar-absorbing coatings and electromagnetic shielding systems.

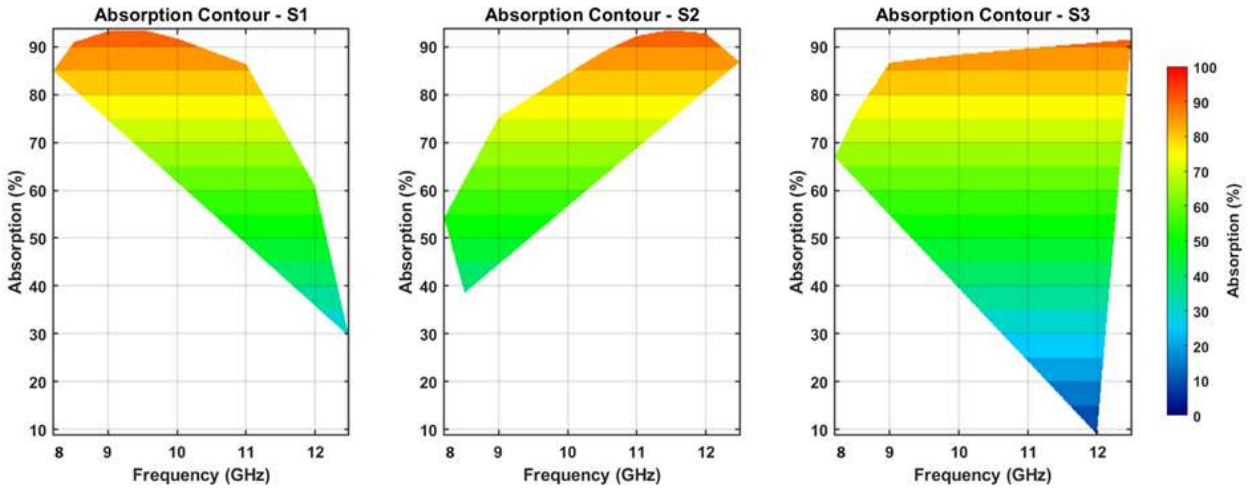

Fig. 6. Absorption contour of three samples in percentag

5.3. Reflection

A quantitative analysis of the reflection data from three NbC–Al_2O_3 composite samples in the 8.2–12.5 GHz range shows a strong dependence of their electromagnetic behavior on the ratio of their constituent components (Figure 7). Sample No.1, which is dominated by the NbC conductive phase, exhibits a clear dipole-frequency trend. Its reflectance decreases from 15.14% at 8.2 GHz to a minimum of 6.31% at 9.5 GHz—the optimal impedance-matching region. It then rises sharply to a maximum of 70.80% at 12.5 GHz, indicating significant mismatch at higher frequencies and the increasing influence of NbC plasmonic effects.

Sample No.2 shows an opposite trend due to its dominant dielectric properties. Its maximum reflectance, 61.66%, occurs at 8.5 GHz as a result of low-frequency dielectric mismatch. From there, the reflectance gradually decreases to a minimum of 6.31% at 11.5 GHz (the dielectric resonance region), followed by a slight increase to 13.10% at 12.5 GHz. Sample No.3, with a more balanced composition, demonstrates the most stable behavior. Its reflectance begins at 33.11% at 8.2 GHz and fluctuates between 11.48% and 20% in the mid-range of 9–11.5 GHz (a relatively well-matched region). However, it then shows a sharp peak of 96.20% at 12 GHz—likely caused by morphological resonance or particle-size effects—followed by a sudden drop to 8.27% at 12.5 GHz. A comparison of the contour plots reveals that sample No.1's reflection depth distribution is highly frequency-dependent, while sample No.2 shows a smoother variation, and sample No.3 displays more pronounced local inhomogeneities. This distinct frequency behavior suggests that sample No.1 is suitable for narrowband applications in the 9–10 GHz region, sample No.2 performs better at frequencies above 10.5 GHz, and sample No.3 is ideal for broadband operation with tolerance to local structural variations. An analysis of the slope of the curves shows that sample No.1 has the steepest changes, with a slope of 64.49% between 9.5 and 12.5 GHz. In contrast, sample No.2 shows a more gradual transition, with a slope of 55.35% from 8.5 to 11.5 GHz. Sample No.3, despite its relative stability across most of the spectrum, demonstrates the most abrupt local shift—an 84.72% jump between 11.5 and 12 GHz. This underscores the importance of precise material-composition control and the need to account for nonlinear behavior when designing absorber systems. Finally, the average reflectance across the full frequency range for samples No.1, No.2, and No.3 is 24.17%, 22.74%, and 25.13%, respectively. These results indicate that the electromagnetic performance of NbC–Al_2O_3 composites is strongly governed by interfacial polarization and microstructural connectivity. The coexistence of conductive and dielectric domains enables tunable loss mechanisms, including eddy-current dissipation and dipolar relaxation. The nonmonotonic reflection behavior observed near 12 GHz further suggests the presence of localized resonance phenomena, likely driven by particle clustering and size dispersion. The differences in slope among the samples reflect the transition from conduction-dominated to polarization-dominated regimes, emphasizing the role of balanced composition in achieving broadband attenuation. Thus, optimizing the NbC-to-Al_2O_3 ratio not only adjusts impedance matching but also allows control over resonance strength and bandwidth. Taken together, these findings highlight the potential of NbC–Al_2O_3 composites.

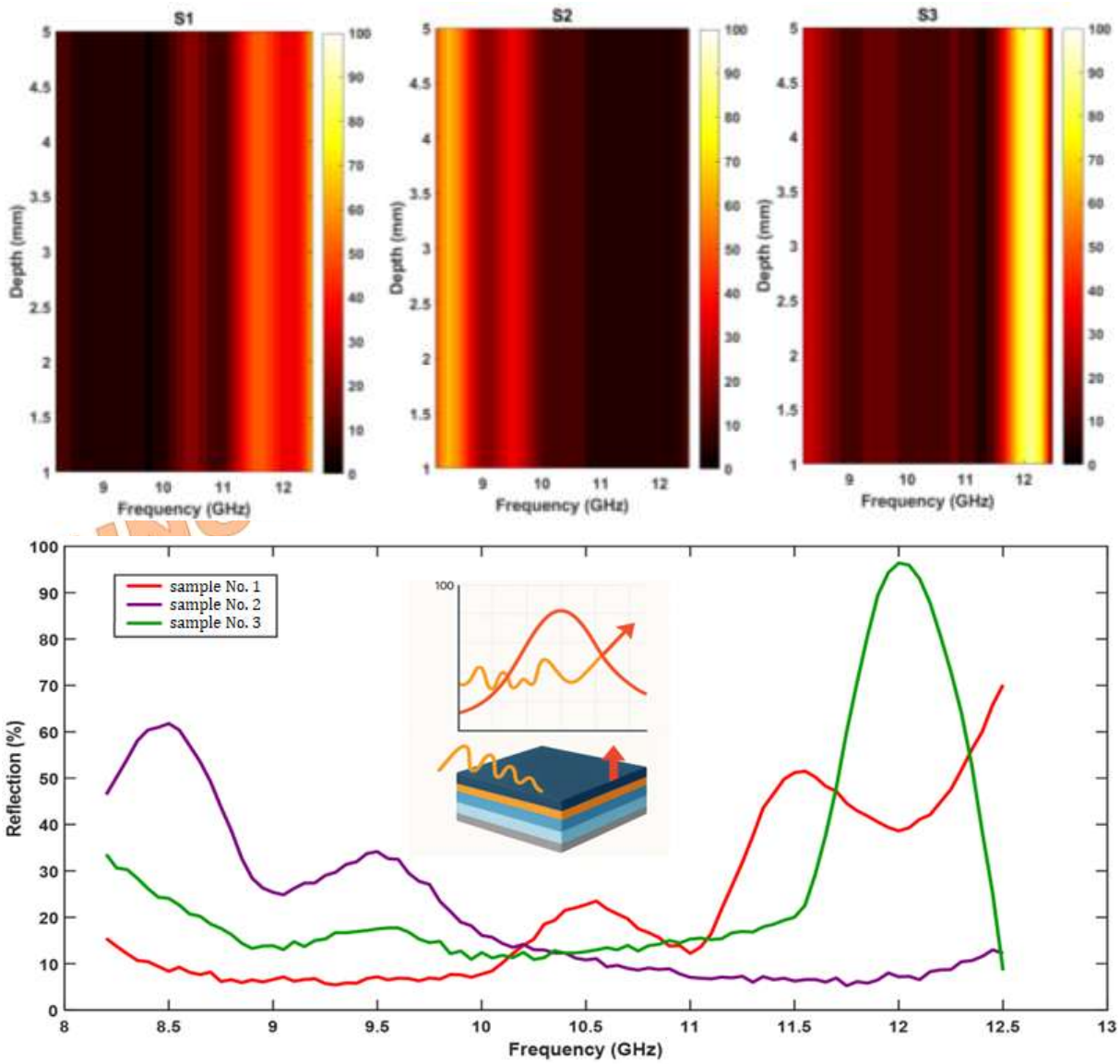

Fig. 7. Reflectance chart in percentage for three composite samples

as adaptive electromagnetic absorbers with frequency-selective capabilities.

5.4. Smith Chart Impedance Matching

Examination of the impedance behavior of the three composite samples on the Smith Chart within the 8.2–12.4 GHz frequency range reveals distinct electromagnetic matching patterns that reflect fundamental differences in their microscopic structure and composition. Sample No.1 shows favorable resonant behavior, achieving maximum matching at 9.5–10 GHz ($|\Gamma|$ = 0.251). This indicates an optimal balance between electrical permittivity and magnetic permeability in this region. Its trajectory on the Smith Chart moves from the high-impedance region toward the center of the circle and then shifts toward the mismatch region ($|\Gamma|$ = 0.841 at 12.5 GHz), illustrating the frequency-dependent variation of its dielectric properties.

Sample No.2 displays a frequency-dependent performance characterized by continuous improvement from low to high frequencies. It transitions from poor matching at 8.5 GHz ($|\Gamma|$ = 0.676) to excellent matching at 11.5–12 GHz ($|\Gamma|$ = 0.251). This behavior suggests a dielectric dispersion mechanism and shows that the presence of Al_2O_3 with reduced NbC content yields better impedance matching in the upper portion of the band. The impedance trajectory of this sample moves smoothly from the edge of the Smith Chart toward the center, indicating decreasing reflection and enhanced absorption as frequency increases.

In contrast, sample No.3—despite having the same Al_2O_3–NbC composition—exhibits unexpected and unstable impedance behavior. It

shows a sharp discontinuity at 12 GHz (|Γ| = 0.955), representing near-complete energy reflection, followed by a sudden recovery at 12.5 GHz (|Γ| = 0.288). This irregular response suggests the presence of spurious resonances, nonuniform distribution of active particles, or structural defects originating from the fabrication process, all of which can compromise the control of electromagnetic properties. Figure 8 and Table 3 present the scattering-parameter values, including reflection loss (RL) and impedance, across the entire frequency range.

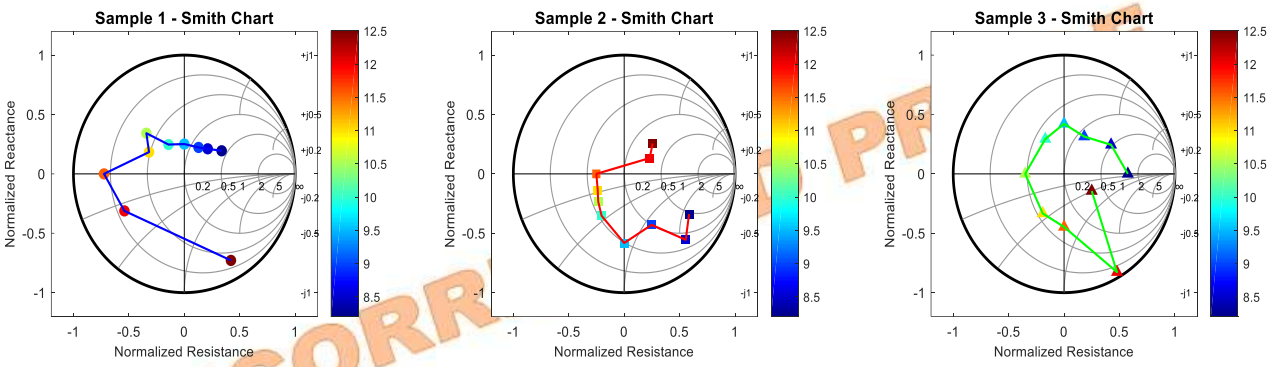

Fig. 8. Impedance matching chart of three samples

Table 3. Reflection loss and impedance matching values of samples in the X-Band

Frequency (GHz)	sample No.1		sample No.2		sample No.3	
	RL(dB)	(|Γ|)	*RL*(dB)	(|Γ|)	*RL*(dB)	(|Γ|)
8.2	-8.2	0.389	-3.4	0.676	-4.8	0.575
8.5	-10.5	0.299	-2.1	0.785	-6.2	0.490
9	-11.8	0.257	-6.1	0.495	-8.8	0.363
9.5	-12	0.251	-4.7	0.582	-7.5	0.422
10	-10.9	0.285	-7.8	0.407	-9.4	0.339
10.5	-6.3	0.484	-9.6	0.331	-9.1	0.351
11	-8.7	0.367	-11.2	0.25	-8.3	0.385
11.5	-2.8	0.724	-12	0.251	-7	0.447
12	-4.1	0.624	-11.5	0.266	-0.4	0.955
12.4	-1.5	0.841	-8.8	0.363	-10.8	0.288

5.5. Composite Properties

Figure 9 presents the X-ray diffraction (XRD) patterns of the three NbC–Al_2O_3 composite samples within the 2θ range of 20°–80°. Each sample displays several characteristic diffraction peaks corresponding to the crystalline phases of NbC and Al_2O_3. In sample No.1, the most prominent peak appears at 2θ ≈ 36° with an intensity of approximately 16,000 counts per second (cps), attributed to the (111) plane of the NbC phase. Additional reflections at 42° and 60.5°, with intensities near 12,000 cps and 8,000 cps, respectively, further confirm the dominance of NbC. Peaks associated with Al_2O_3 are detected at 25.5° and 28.5°, showing lower intensities (up to about 6,000 cps), which indicates that aluminum oxide contributes less significantly in this composition. In sample No.2, with an increased Al_2O_3 content, the peak at 28.5° becomes more intense (≈ 9,000 cps), and the 25.5° reflection is also more pronounced compared to sample No.1. Meanwhile, the main NbC peak at 36° slightly decreases in intensity to around 15,000 cps, suggesting a relative reduction in the NbC phase fraction. Sample No.3, containing an approximately equal ratio of NbC and Al_2O_3, exhibits a more balanced diffraction pattern. In this case, the 36° peak for NbC and the 28.5° peak for Al_2O_3 show comparable intensities of roughly 14,000 cps and 10,000 cps, respectively. A minor overlap of NbC and Al_2O_3 reflections in the 37°–45° region is observed in all

samples and varies with composition. High-angle reflections at 66.5° and 77° are more distinct in the third sample, reflecting the more comparable contributions of both phases at higher crystallographic orientations. Overall, as the Al_2O_3 content increases, the intensity of its characteristic peaks consistently rises across the angular range, while the NbC peaks gradually weaken. This trend highlights the compositional dependence of the crystalline phases and provides a reliable means to monitor variations in phase ratios among the composites. A closer inspection of the diffraction peak profiles reveals noticeable broadening with increasing Al_2O_3 content, indicating a progressive reduction in crystallite size and the development of interfacial strain. The estimated crystallite size of the NbC phase decreases from approximately 45 nm in sample No.1 to around 35–37 nm in Sample No.3, demonstrating that the incorporation of Al_2O_3 restricts grain coarsening and induces localized lattice distortion. This microstructural refinement increases the interfacial area and can enhance polarization and scattering losses, consistent with the electromagnetic performance discussed earlier.

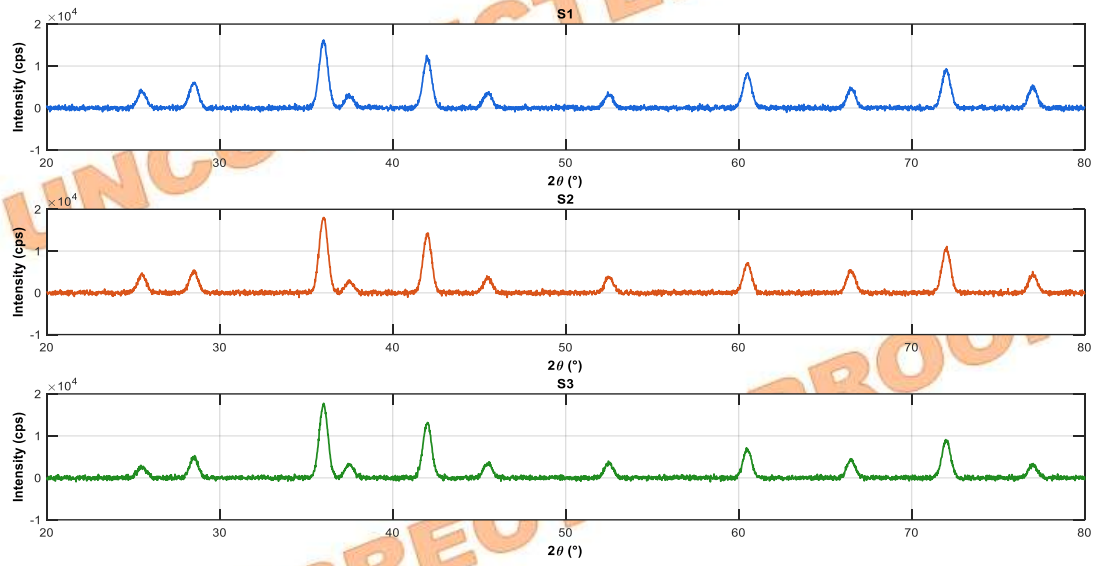

Fig. 9. XRD patterns of nano-composite samples (CPS vs. 2θ)

Figure 10 presents the scanning electron microscopy (SEM) micrographs of the three composite samples obtained at magnifications of 2 µm and 5 µm. These images reveal a relatively uniform distribution of NbC and Al_2O_3 particles, with the degree of agglomeration decreasing as the Al_2O_3 fraction increases. The finer dispersion and smoother morphology observed in the third sample confirm the improved homogeneity and reduced particle clustering inferred from the XRD analysis. Moreover, the SEM micrographs highlight the presence of interfacial contact between NbC and Al_2O_3 grains, which can enhance charge transfer and local polarization effects. The variation in particle packing and intergranular spacing is likely to contribute to increased scattering and absorption of electromagnetic waves within the composite matrix.

The simulated FTIR spectra of the NbC/Al_2O_3/epoxy composites, before and after silane surface modification, show distinct differences in their transmittance profiles(Figure 11). Compared to the unmodified composite, the silanized nano-composite displays deeper absorption bands, indicating stronger interactions between the nanoparticles and the epoxy matrix. The O–H stretching vibration at ~3300 cm^{-1} exhibits a noticeable increase in intensity after surface treatment, reflecting enhanced hydrogen bonding and improved surface hydroxyl functionalization. The C–H stretching bands at 2920 and 2850 cm^{-1} are also moderately intensified, suggesting successful incorporation of organic silane groups. The carbonyl band at 1720 cm^{-1} becomes more pronounced, pointing to improved crosslinking density and enhanced compatibility between the resin and the fillers. The characteristic Si–O–Si network peaks at 1100 and 1030 cm^{-1} show a significant increase, directly confirming the formation of silane bonds on the NbC and Al_2O_3 surfaces. Additionally, a slight shift and sharpening of the epoxy-related band at 910 cm^{-1} indicate improved interfacial adhesion. Overall, the comparison between the spectra before and after silane treatment demonstrates that surface modification enhances nanoparticle dispersion, strengthens the polymer–filler network, and improves the composite's potential EMI shielding performance. The reduced baseline noise and the sharper, well-defined peaks in the silanized

spectrum reflect more uniform interactions within the material. These spectral features collectively confirm the effectiveness of the surface modification process and its direct impact on the structural properties of the nano-composite.

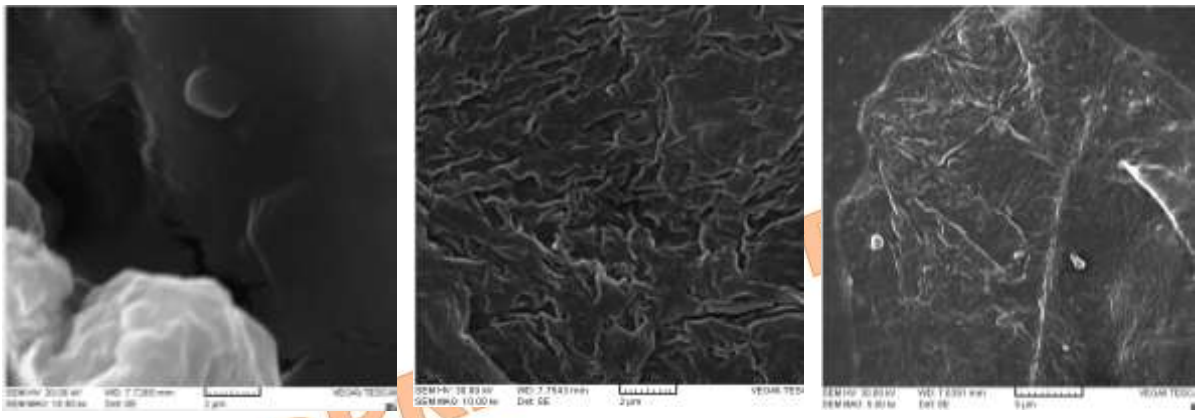

Fig. 10. SEM images of the particle distribution in the matrix for nano-composite samples at different scales (μm)

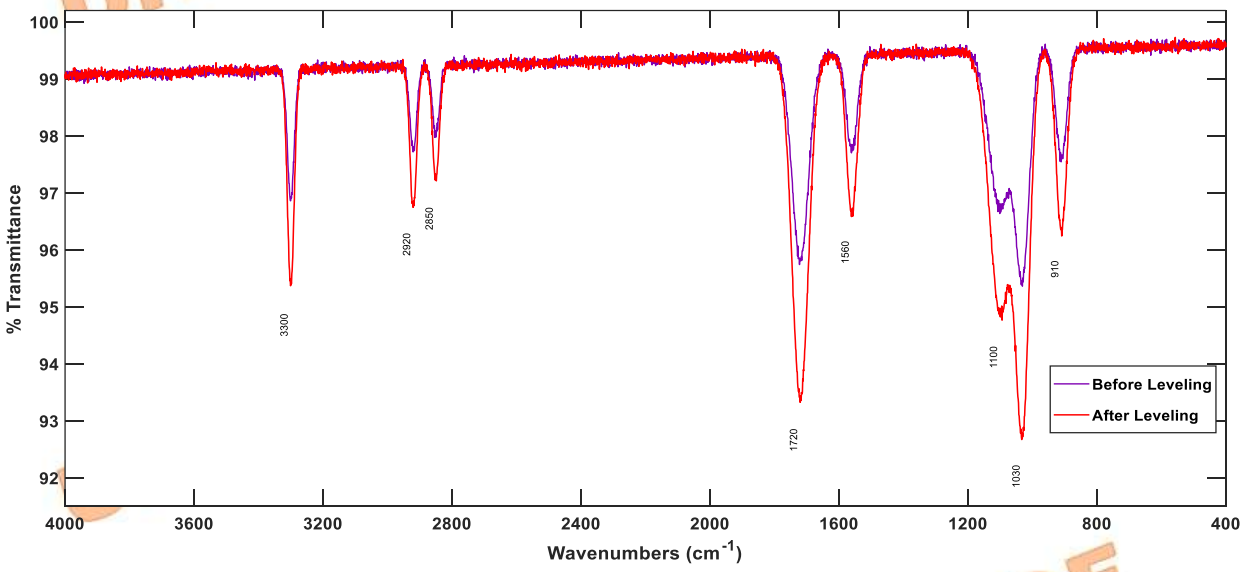

Fig. 11. FTIR (KBr) spectra of the samples before and after silane surface treatment (Transmittance vs. Wavenumber)

6. Summary and Conclusions

This section summarizes the findings from the fabrication and evaluation of polymer nano-composites designed for electromagnetic wave absorption in the X-band frequency range. The novelty of this research lies in the simultaneous incorporation of NbC and Al_2O_3 phases at varying ratios within an epoxy resin matrix, combined with a silane surface treatment to enhance chemical bonding and optimize phase integration. Chemical and structural characterizations, including XRD, FTIR, and SEM, were employed to verify particle dispersion, phase interactions, and the effectiveness of the surface treatments. A comprehensive analysis of absorption and reflection behaviors revealed that the phase ratio strongly influences both the location and intensity of absorption peaks. Sample No.1, with a NbC: Al_2O_3 ratio of 4:3, demonstrated optimal mid-band performance, achieving a minimum *RL* of −12 dB at 9.5 GHz and over 90% absorption between 9.5 and 10.5 GHz, though its reflectance rose to approximately 70% at higher frequencies. Sample No.2, with a 3:4 ratio, exhibited more stable absorption in the upper frequency range, achieving an *RL* minimum of −12 dB at 11.5 GHz and maintaining over 80% absorption from 9 to 12 GHz, reflecting improved impedance matching with Al_2O_3-rich compositions. Sample No.3, with an equal 1:1 ratio, showed a more uniform response, with multiple absorption peaks ranging from 85% to 92% and an *RL* minimum of −10.8 dB at 12.5 GHz. Impedance analysis using the Smith Chart revealed distinct matching behaviors: Sample No.1 showed favorable resonance at 9.5–10 GHz ($|\Gamma|$ = 0.251), sample No.2 exhibited gradual

improvement from 8.5 GHz (|Γ| = 0.676) to 11.5–12 GHz (|Γ| = 0.251), and sample No.3 displayed a sharp impedance break at 12 GHz (|Γ| = 0.955) followed by recovery at 12.5 GHz (|Γ| = 0.288), indicating minor structural inhomogeneities. Absorption contour analysis showed sample No.1 with a narrow but strong matching region, sample No.2 with a broad absorption bandwidth, and sample No.3 with multiple resonances and intermittent drops. Increasing NbC content shifted absorption toward the mid-band, while higher Al_2O_3 ratios moved absorption to higher frequencies. This trend was corroborated by XRD and FTIR analyses, which confirmed phase distribution and the formation of chemical bonds via silane treatment. Sample No.1 had a dominant NbC peak at 36° (~16,000 cps), sample No.2 showed an enhanced Al_2O_3 peak at 28.5° with reduced NbC intensity (~9,000 cps), and sample No.3 displayed balanced peak intensities.

These results indicate that sample No.1 is suitable for mid-frequency absorption, sample No.2 for upper frequency ranges, and sample No.3 for uniform and stable absorption across the entire measured range, highlighting the novelty of the dual-phase NbC/Al_2O_3 system combined with optimized surface treatment for broadband electromagnetic wave attenuation. Figure 12 illustrates the roles of NbC in conduction loss and Al_2O_3 in interfacial polarization.

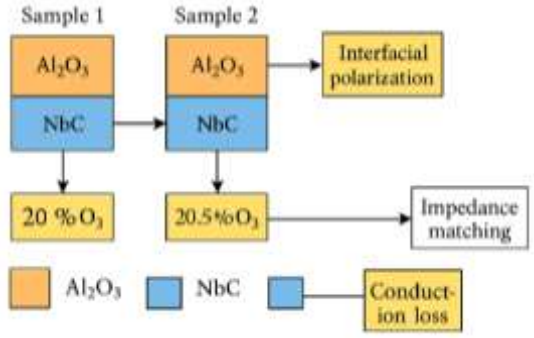

Fig. 12. Effects of NBC surface polarization and dielectric loss for samples No.1 and No.2

6.1. Limitations and Future Researches

This study examined the reflection and absorption performance of a silane-treated dual-phase NbC–Al_2O_3 nano-composite embedded in a resin matrix with a specific thickness in the X-band. The results showed strong attenuation and good impedance matching; however, the experiments were limited to a single thickness and measurements taken at normal incidence within a rectangular waveguide. Other angles of incidence were not explored. Future research could investigate absorption performance at various angles, as well as alternative porous and ceramic materials that could provide greater microwave attenuation. Expanding the study to include multi-layer or graded structures and to other frequency bands, such as C and Ku, would also improve broadband and angle-insensitive performance. Furthermore, evaluating thermal stability and long-term environmental durability will be crucial for practical applications in radar and stealth technology.

Acknowledgments

This research received support from the tools and equipment provided by the Faculty of Chemical, Electrical, and Mechanical Engineering, Iran University of Science and Technology.

Funding Statement

This research did not receive any specific grants from funding agencies in the public, commercial, or not-for-profit sectors.

Conflicts of Interest

The author declares that there is no conflict of interest in the publication of this article.

References

[1] Shao, T., Ma, H., Wang, J., Feng, M., Yan, M., Wang, J., Yang, Z., Zhou, Q., Luo, H. and Qu, S., 2020. High-temperature absorbing coatings with excellent performance combine Al2O3 and TiC materials. Journal of the European Ceramic Society, 40(5), pp. 2013-2019.

[2] Meng, F., Wang, H., Huang, F., Guo, Y., Wang, Z., Hui, D., and Zhou, Z., 2018. Graphene-based microwave absorbing composites: A review and perspective. Composites Part B: Engineering, 137, pp. 260-277.

[3] Kim, J.B., Lee, S.K., and Kim, C.G., 2008. Comparison study on the effect of carbon nano materials for single-layer microwave absorbers in X-band. Composites Science and Technology, 68(14), pp. 2909-2916.

[4] Wang, H., Zhu, D., Zhou, W., and Luo, F., 2015. High temperature electromagnetic and microwave absorbing properties of polyimide/multi-walled carbon nanotubes nanocomposites. Chemical Physics Letters, 633, pp. 223-228.

[5] Qing, Y., Zhou, W., Luo, F., and Zhu, D., 2017. Thin-thickness FeSiAl/flake graphite-filled Al_2O_3 ceramics with enhanced microwave absorption. Ceramics International, 43(1), pp. 870-874.

[6] Zhou, L., Zhou, W., Su, J., Luo, F., Zhu, D. and Dong, Y., 2012. Plasma-sprayed Al_2O_3/FeCrAl composite coatings for electromagnetic wave absorption application. Applied Surface Science, 258(7), pp. 2691-2696.

[7] Zhao, Y.P., Hu, Y., Yang, Y., Wang, Y.W., Wang, X.Y., Li, W., Shao, Y.X., Sun, W.W., Zhao, H.J. and Ma, Y.D., 2025. Microstructure and properties of plasma-sprayed NbC-Al_2O_3 composite coatings. Ceramics International, 50(24), pp. 54955-54965.

[8] Wang, X.Y., Yang, W., Shao, Y.X., Yang, Y., Yang, Z.L., Wang, Y.W., Cui, Y.H., Ma, Y.D., Sun, W.W. and Li, W., 2021. Effect of nano-Al_2O_3 on the microstructure and properties of NbB_2-NbC composite coatings prepared by plasma spraying. Journal of the American Ceramic Society, 104(12), pp. 6477-6488.

[9] Liang, H.E., Yang, Y., Wang, X.L., Yang, Z.L., Li, W., Wang, Y.W. and Shao, Y.X., 2024. TEM characterization and toughening mechanism of in-situ NbB_2-NbC-Al_2O_3 composite coatings prepared by plasma spraying. Materials Characterization, 210, pp. 113783.

[10] Mei, H., Yang, D., Yang, W., Yao, L., Yao, Y., Cheng, L. and Zhang, L., 2021. 3D-Printed Impedance Gradient Al_2O_3 Ceramic with in-Situ Growing Needle-like SiC Nanowires for Electromagnetic Wave Absorption. Ceramics International, 47(22), pp. 31990-31999.

[11] Cai, R., Zheng, W., Yang, P., Rao, J., Huang, X., Wang, D., Du, Z., Yao, K., and Zhang, Y., 2022. Microstructure, Electromagnetic Properties, and Microwave Absorption Mechanism of SiO_2-MnO-Al_2O_3 Based Manganese Ore Powder for Electromagnetic Protection. Molecules, 27(12), pp. 3758.

[12] Trung, V.Q., Tung, D.N. and Huyen, D.N., 2009. Polypyrrole/Al_2O_3 nanocomposites: preparation, characterisation and electromagnetic shielding properties. Journal of Experimental Nanoscience, 4(3), pp. 213-219.

[13] Wen, L., Zhang, J., Guan, L., Zhu, Y., Zhao, B., Song, L., Zhu, X., and Zhang, R., 2024. Natural bamboo-derived NbC nanowires for efficient electromagnetic wave absorption. Journal of the American Ceramic Society, 107(4), pp. 2453-2465.

[14] Delgado, N., Salas, O., Garcés, E. and Magaña, L.F., 2023. Ab-Initio Calculation of the Electrical Conductivity, Optical Absorption, and Reflectivity of the 2D Materials SnC and NbC. Crystals, 13(4), pp. 682.

[15] Wei, B., Wang, Y., Zhao, Y., Wang, D., Song, G., Fu, Y. and Zhou, Y., 2018. Effect of NbC content on microstructure and mechanical properties of W-NbC composites. International Journal of Refractory Metals and Hard Materials, 70, pp. 66-76.

[16] Fang, L., Yan, H., Yao, Y., Zhang, P., Gao, Q., and Qin, Y., 2018. Reactive Fabrication and Effect of NbC on Microstructure and Tribological Properties of CrS Co-Based Self-Lubricating Coatings by Laser Cladding. Materials, 11(1), pp. 44.

[17] Song, X., Li, Y., Zhang, H., Wang, Q., and Chen, J., 2024. Mechanical Properties of a Honeycomb Structure Dispersed with 3D-Printed Fe_3O_4 Nanomaterials. ACS Omega, 9(12), pp.14287–14296.

[18] Xu, L., Wang, W., Liu, Y. and Liang, D., 2022. Nanocellulose-Linked MXene/Polyaniline Aerogel Films for Flexible Supercapacitors. Gels, 8, pp.798

[19] Zhao, H., Ma, X., Li, C., Song, X., Fu, Y., and Gao, B., 2025. Study on the Electromagnetic Absorption Optimization Design of Honeycomb Structures with Ti3C2Tx/Fe3O4/UV Resin. Journal of Alloys and Compounds, pp.182180.

[20] Guo, S., Guo, Y., Wang, T., Zhang, T., Zhao, D., Fan, F., Yang, X., Song, X., and Fu, Y., 2025. Study on the optimization of electromagnetic absorption and mechanical properties of 3D printed γ-Fe2O3/UV Resin-Based honeycomb structures. ACS Applied Electronic Materials, 7(2), pp.766-778.

[21] Li, C. and Song, X., 2023. Surface size-and structure-optimized design of two-dimensional MXene nanosheets for electromagnetic wave absorption. ACS Applied Nano Materials, 6(13), pp.12050-12062.

[22] Yang, Z., Sun, M., Li, J., Zhou, Q., Ren, W., and Jia, Y., 2021. Microwave-absorbing performance of a radar-absorbing structure composed of K0. 5Na0. 5NbO3/ZrO2/Al2O3 heterojunction. Ceramics International, 47(22), pp.31811-31816.

[23] Gogoi, D., Korde, R., Chauhan, V.S., Patra, M.K., Roy, D., Das, M.R., and Ghosh, N.N., 2022.

CoFe2O4 nanoparticles grown within porous Al2O3 and immobilized on graphene nanosheets: a hierarchical nanocomposite for broadband microwave absorption. ACS omega, 7(32), pp.28624-28635.

[24] Ye, X., Zhang, Y., Xu, J., Li, S., Ma, X., Cao, L., Zhang, J., Zhang, X. and Zheng, K., 2025. Synergistic enhancement of radar wave absorption in SiC/Al2O3 composites via structural tuning, composition optimization, and unit design. Materials Today Physics, 51, pp.101662.

[25] Rezaei Qazviniha, M. and Piri, F., 2023. Synthesis and characterization of Al2O3/novolac/fiberglass nanocomposite: Modification of thermal stability and thermal insulation properties. Mechanics Of Advanced Composite Structures, 10(1), pp.21-28.

[26] Ye, X., Zhang, Y., Xu, J., Li, S., Ma, X., Cao, L., Zhang, J., Zhang, X. and Zheng, K., 2025. Synergistic enhancement of radar wave absorption in SiC/Al2O3 composites via structural tuning, composition optimization, and unit design. Materials Today Physics, 51, pp.101662.

[27] Fang, X., Wu, Q., Gu, Z., Ma, H., Yin, S., Tong, R., Liu, L., and Zuo, R., 2025. Compositionally tailoring dielectric properties of MCMB-SiC/Al2O3 porous composites for enhanced microwave absorption. Materials Today Communications, pp.113659.

[28] Paul, A., Kt, A., George, P.P., and George, M., 2025. Biowax-derived epoxy composites with rGO–NZF–Al_2O_3: a green solution for enhanced EMI shielding and structural performance. Composite Interfaces, pp.1-21.

[29] Rashidi, A., Kiyani, G. and Nosrati, R., 2021. A review of the mechanism and performance of electromagnetic wave absorbers made of polymer nanocomposites. Journal of the Iranian Electrical and Electronic Engineering Association, 18(4), pp. 1-15.

[30] Chen, D., Wang, G.S., He, S., Liu, J., Guo, L., and Cao, M.S., 2013. Controllable Fabrication of Mono-Dispersed RGO–Hematite Nanocomposite and Their Enhanced Wave Absorption Properties. Journal of Materials Chemistry A, 1(19), pp. 5996-6003.

[31] Huang, B., Yue, J., Wei, Y., Huang, X., Tang, X., and Du, Z., 2019. Enhanced Microwave Absorption Properties of Carbon Nanofibers Functionalized by FeCo Coatings. Applied Surface Science, 483, pp. 98-105.

[32] Gao, S., Zhang, Y., Xing, H., and Li, H., 2020. Controlled reduction synthesis of yolk-shell magnetic@ void@ C for electromagnetic wave absorption. Chemical Engineering Journal, 387, pp.124149.

[33] Markel, V.A., 2016. Introduction to the Maxwell Garnett approximation: tutorial. Journal of the Optical Society of America A, 33(7), pp.1244-1256.

[34] Sarkhosh, R., Kazemi Nasrabadi, M., and ParsaFar, R., 2024. Study of the effect of fumed silica on the mechanical, electrical, and magnetic properties of epoxy/fumed silica composite. Iranian Journal of Manufacturing Engineering, 11(2), pp.37-57.